Chinese Chemical Letters 36 (2025) 110567

Contents lists available at ScienceDirect

Chinese Chemical Letters

journal homepage: www.elsevier.com/locate/cclet

Triple-conducting heterostructure anodes for electrochemical ethane nonoxidative dehydrogenation by protonic ceramic electrolysis cells

Yixin Lu, Minghan Qin, Shixian Zhang, Zhen Liu, Wang Sun*, Zhenhua Wang*, Jinshuo Qiao, Kening Sun

Beijing Key Laboratory of Chemical Power Source and Green Catalysis, School of Chemistry and Chemical Engineering, Beijing Institute of Technology, Beijing 100081, China

ARTICLE INFO

Article history:
Received 17 July 2024
Revised 15 October 2024
Accepted 17 October 2024
Available online 19 October 2024

Keywords:
Protonic ceramic electrolysis cells
Anode
Ethylene
Electrochemical ethane nonoxidative dehydrogenation
Heterostructure

ABSTRACT

In response to the increasing demand of ethylene, electrochemical ethane nonoxidative dehydrogenation (EENDH) to ethylene by protonic ceramic electrolysis cells (PCECs) is developed. However, existing anode materials exhibit poor proton conductivity and limited catalytic activity. Herein, a novel $Sr_{1.95}Fe_{1.4}Co_{0.1}Mo_{0.4}Zr_{0.1}O_{6-\delta}$ (SFCMZ) anode is prepared as PCECs anode for EENDH. Zr doping increases the oxygen vacancies and enhances the proton conductivity of SFCMZ. Moreover, an alloy-oxide heterostructure (CoFe@SFCMZ) is formed through *in-situ* exsolution of CoFe alloy nanoparticles under reduction conditions, generating abundant oxygen vacancies and improving its catalytic activity. CoFe@SFCMZ cell achieves an electrolysis current density of 0.87 A/cm^2 at 700 °C under 1.6 V, with an ethane conversion rate of 34.22% and corresponding ethylene selectivity of 93.4%. These results demonstrate that CoFe@SFCMZ anode exhibits excellent electrocatalytic activity, suggesting promising applications for EENDH.

Ethylene is one of the most widely produced organic compounds globally, extensively used in the production of various chemical intermediates and polymers [1,2]. Currently, ethylene is primarily produced by the steam cracking of ethane and naphtha, which is an energy-intensive and high-carbon-emitting process, typically every ton of produced ethylene emits 1–2 tons of CO_2 and consumes 17–21 GJ of energy [3,4]. Additionally, there are severe coking issues in this process, and adverse side reactions may result in the emission of pollutants [5]. In order to save energy and alleviate carbon deposition during ethane cracking, the ethane oxidative dehydrogenation (EODH) method is proposed [6]. However, due to the propensity for deep oxidation of ethylene, this process must be conducted at low conversion rates to achieve higher selectivity [7,8]. Furthermore, the safety hazards associated with mixing ethane and oxygen need to be considered. The ethane nonoxidative dehydrogenation (ENDH) can overcome these issues of EODH. But ENDH faces the challenge of separating C_2H_4 and H_2 in the product stream, leading to low ethane conversion rate and ethylene selectivity, as well as rapid catalyst deactivation due to coking [9,10].

In recent years, protonic ceramic electrolysis cells (PCECs) have attracted widespread attention in the field of energy conversion and storage [11-13]. PCECs can synthesize diversified chemicals through the combination of renewable electricity and waste heat, reducing carbon footprint and improving energy efficiency [14]. When utilized as electrochemical ethane nonoxidative dehydrogenation (EENDH) reactors, PCECs enable efficient reaction and product separation. C_2H_6 is introduced on the anode and undergoes electrochemical dehydrogenation reaction to convert into C_2H_4 and H^+ (Eq. 1), and the generated electrons pass through the external circuit to the cathode. H^+ is conducted from the anode side to the cathode side through the proton conducting electrolyte under the action of applied voltage, where it reacts with CO_2 to generate CO and H_2O (Eq. 2). By manipulating the operating temperature and voltage, PCECs can offer flexible adjustment of ethane conversion rate and ethylene selectivity [15].

$$C_2H_6 \rightarrow C_2H_4 + 2H^+ + 2e \quad (1)$$

$$CO_2 + 2H^+ + 2e^- \rightarrow CO + H_2O \quad (2)$$

Improving anode materials is one of the crucial challenges for PCECs performance breakthroughs [16,17]. The most common PCECs anode is Ni-cermet anode which has good catalytic performance, but in the ethane dehydrogenation reaction, Ni metal

* Corresponding authors.
E-mail addresses: sunwang@bit.edu.cn (W. Sun), wangzh@bit.edu.cn (Z. Wang).

https://doi.org/10.1016/j.cclet.2024.110567
1001-8417/

will cause deep cracking of ethane, resulting in low ethylene selectivity and carbon deposition [18]. Recently, the perovskite oxides have become candidate anode materials due to their excellent anti coking stability and mixed ion-electron conductivity [19-22]. However, the catalytic activity of perovskite oxides is much lower than that of Ni-cermet anodes. To further enhance the electrocatalytic performance of perovskite oxides, forming a metal-oxide heterostructure is an effective way. *In-situ* exsolution of active metal nanoparticles under reducing conditions can generate a large number of uniformly distributed nanoparticles on the surface, providing more catalytic active sites [23,24]. Moreover, nanoparticles are firmly anchored on the substrate surface to form micro-nano heterostructures, which not only synergistically enhance catalytic activity but also effectively inhibit particle aggregation [25-27]. We prepared $Sr_{1.95}Fe_{1.4}Co_{0.1}Mo_{0.5}O_{6-\delta}$ and induced *in-situ* exsolution of CoFe alloy, forming an alloy-oxide heterostructure (CoFe@SFCoM) with abundant reactive sites. The single cell with CoFe@SFCoM anode exhibited an ethane conversion of 36.4% and an ethylene selectivity of 94.5% at 800 °C based on ethane oxidative dehydrogenation by solid oxide electrolysis cells [28].

Besides, C_2H_6 is converted into C_2H_4 and H^+ on the PCECs anode, and the traditional perovskite oxides are typical mixed conductors of oxygen ions and electrons, which exhibit limited proton conductivity and catalytic activity. Studies have shown that introducing proton conduction to form oxygen ion-proton-electron triple-conducting oxides extends the electrochemical active sites from the three-phase interface to the entire anode surface, which is an effective approach to addressing the above-mentioned issues [29,30]. The proton transport in perovskite oxides primarily involves proton absorption (hydration reaction) as well as inter- and intra-lattice movement (including jumping and rotation) [31]. Proton absorption can lead to the formation of protonic carriers $OH_O^{\cdot}$ by incorporating H_2O or H into oxygen vacancies, as shown in Eq. 3 [32,33]. Therefore, increasing oxygen vacancy has been proved to be an effective strategy to promote proton conduction [34].

$$H_2O + V_O^{\cdot\cdot} + O_O^{\times} \leftrightarrow 2OH_O^{\cdot} \quad (3)$$

Herein, we design $Sr_{1.95}Fe_{1.4}Co_{0.1}Mo_{0.4}Zr_{0.1}O_{6-\delta}$ (SFCMZ) perovskite oxide by doping Zr element at B-site of $Sr_{1.95}Fe_{1.4}Co_{0.1}Mo_{0.5}O_{6-\delta}$ (SFCM). Zr doping can significantly increase sufficient oxygen vacancies and boost the spontaneous formation of proton defects, enhancing the proton conductivity of SFCMZ [35]. Furthermore, CoFe alloy nanoparticles are *in-situ* exsolved on the surface of SFCMZ (CoFe@SFCMZ) to deliver strong interface interactions by reducing treatment, thereby enhancing its electrocatalytic activity, as shown in Fig. 1. CoFe@SFCMZ as PCECs anode demonstrates excellent structural stability, enhanced proton conductivity and outstanding electrocatalytic activity for EENDH. This work provides a new design strategy for the development of PCECs anodes, offering a feasible approach for their applications.

X-ray diffraction (XRD) is used to analyze the phase structures of SFCMZ and SFCM and their reduced samples (denoted as SFCMZ-R and SFCM-R, respectively, both are reduced in 5% H_2/Ar atmosphere at 800 °C for 5 h), as shown in Fig. 2a. SFCMZ and SFCM samples present a cubic perovskite structure (PDF #97–009–6233) with a space group of Fm-3m. After reduction, the main phase structures of SFCMZ-R and SFCM-R are unchanged, indicating an excellent structural stability in reducing atmosphere. In addition, a clear characteristic peak of CoFe alloy (PDF #49–1568) is observed near 44.8° in two reduced samples, showing that CoFe alloy is exsolved after reduction to form the alloy-oxide heterostructures (CoFe@SFCMZ and CoFe@SFCM), as shown in Fig. 2b. Moreover, the main peak of SFCMZ (~32.2°) has a smaller angle than that of SFCM, showing a lattice expansion due to the partial substitution of Mo^{6+} (0.42 Å) by Zr^{4+} (0.72 Å) with larger ionic radius [36]. The XRD patterns are further analyzed by Rietveld refinement method, as shown in Fig. S1 (Supporting information). The cell volume of CoFe@SFCMZ is 494.363 $Å^3$, while that of CoFe@SFCM is 490.636 $Å^3$. The increased cell volume after Zr^{4+} substitution is consistent with the shift of the diffraction peak to a small angle. The results also show that the cell volume of CoFe@SFCMZ is larger than that of SFCMZ, which is due to the valence decrease of metal cations after reduction, and the lower the valence of the same cations, the larger the radius.

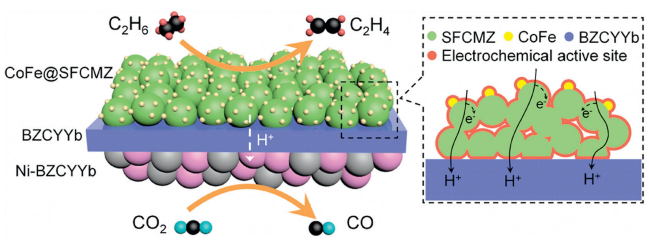

Fig. 1. Schematic diagram of EENDH in PCECs and novel triple-conducting anodes.

The surface morphology of CoFe@SFCMZ sample is shown in Fig. 2c. A large number of uniformly distributed CoFe alloy nanoparticles appear on the surface of SFCMZ matrix with the particle size of ~60 nm, and these exsolved nanoparticles are further confirmed by high-resolution transmission electron microscopy (HR-TEM) (Fig. 2d). The lattice spacing of the exsolved nanoparticles is 0.203 nm, which is consistent with the (110) lattice plane of CoFe alloys. These CoFe nanoparticles are tightly embedded on SFCMZ matrix to form an alloy-oxide heterostructure, while the strong interaction between CoFe alloy nanoparticles and SFCMZ matrix can effectively avoid particle aggregation and extend the electrocatalytic active sites. Furthermore, it can be observed that except for the significant enrichment of Co element (green) and Fe element (purple), other elements are uniformly distributed as shown in Fig. 2e.

Fig. 3a shows the O 1s orbital fitting spectra of CoFe@SFCMZ and CoFe@SFCM samples. It can be observed that there are three characteristic peaks, namely lattice oxygen (O^{2-}, 529.2 eV), adsorbed oxygen (O_2^{2-}/O^-, 531.4 eV) and surface adsorbed carbonate or hydroxyl (CO_3^{2-}/OH^-, 533.3 eV) [37]. And the fitting results are shown in Table S1 (Supporting information). After Zr doping, the proportion of lattice oxygen decreases from 38.73% to 32.92% and the proportion of adsorbed oxygen increases from 58.59% to 60.88%. Zr doping leads to a relatively greater concentration ratio of adsorbed oxygen to lattice oxygen, which suggests that CoFe@SFCMZ contained more oxygen vacancies than CoFe@SFCM [38]. The increased oxygen vacancy concentration may be caused by the charge imbalance when low valence Zr^{4+} replaces high valence Mo^{6+}, which can be represented by the Kroger-Vink symbol equation as follows (Eq. 4) [39]:

$$ZrO_2 + Mo_{Mo}^{\times} + O_O^{\times} \rightarrow Zr_{Mo}^{\cdot\cdot} + V_O^{\cdot\cdot} + MoO_3 \quad (4)$$

The valence state changes of metal elements in CoFe@SFCMZ and CoFe@SFCM samples are also determined by X-ray photoelectron spectroscopy (XPS). Fig. S3a (Supporting information) shows the fitting spectra of Fe 2p orbitals, where Fe elements exist in mixed valence states of Fe^{2+} (~709.9 eV/723.1 eV), Fe^{3+} (~711.2 eV/724.4 eV) and Fe^{4+} (~712.9 eV/726.1 eV) [40]. Besides, a characteristic peak is also found at the position of ~708.8 eV/722.0 eV in both samples, corresponding to the zero valence state of Fe [41]. The average valence state of Fe element in CoFe@SFCMZ sample decreases from 2.84 to 2.80 after Zr doping. Fig. S3b (Supporting information) shows the fitting spectra of Co 2p orbitals, and Co element exists in a mixed valence state of Co^{2+} (780.2 eV) and Co^{3+} (782.8 eV) [42]. And the characteristic peak of the zero valence state of Co is also found around 777.8 eV [43].

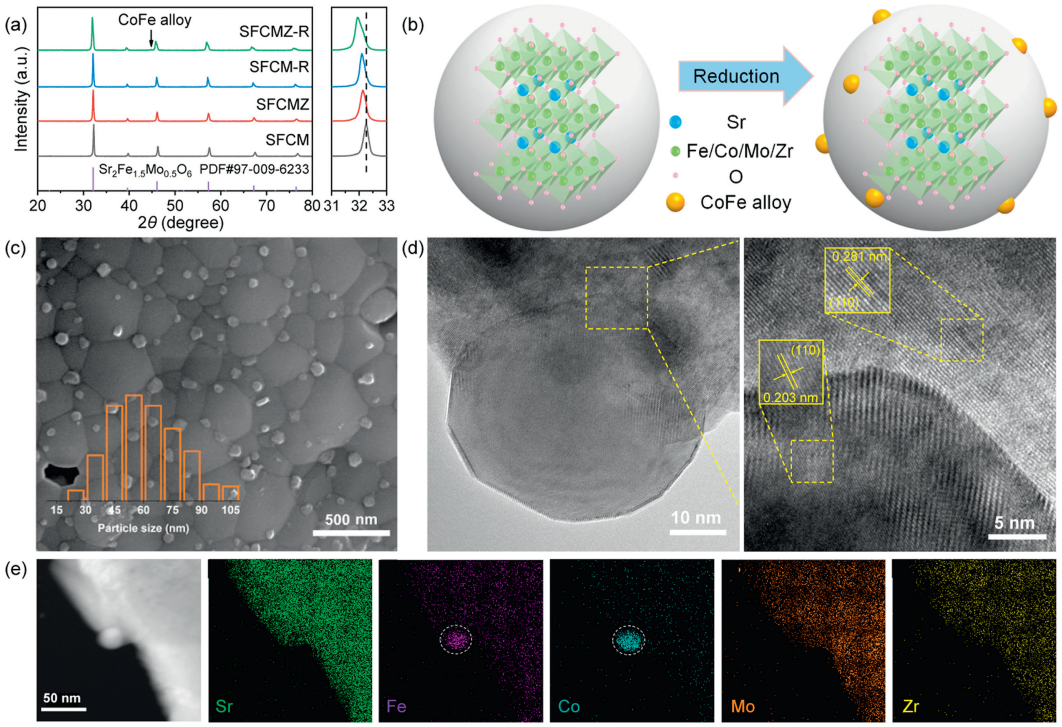

Fig. 2. (a) XRD patterns of SFCM, SFCMZ, SFCM-R and SFCMZ-R powders. (b) Schematic diagram of exsolution process of SFCMZ sample. (c) SEM image of CoFe@SFCMZ. (d) HR-TEM image and local magnification of CoFe@SFCMZ. (e) EDX distribution of CoFe@SFCMZ.

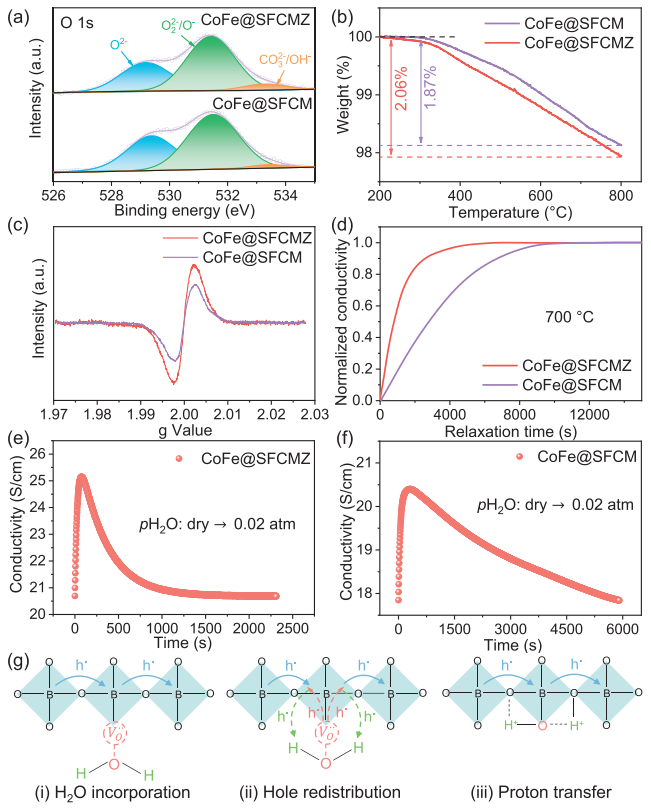

Fig. 3. (a) O 1s XPS spectra of CoFe@SFCMZ and CoFe@SFCM. (b) TGA test diagram of CoFe@SFCMZ and CoFe@SFCM in Ar. (c) EPR test curves of CoFe@SFCMZ and CoFe@SFCM in 5% H_2/Ar. (d) ECR test curves of CoFe@SFCMZ and CoFe@SFCM. Changes of conductivity when switching from dry state to the wet for (e) CoFe@SFCMZ and (f) CoFe@SFCM. (g) Schematic diagram of hydration reaction.

After Zr doping, the average valence state of Co in CoFe@SFCMZ sample decreases from 2.40 to 2.30. The above results indicate the exsolution of Co and Fe elements after reduction, which is consistent with the results of XRD and HR-TEM. Fig. S3c (Supporting information) shows the fitting spectra of Mo 3d orbitals, with four characteristic peaks observed as Mo^{5+} (~232.2 eV/235.4 eV) and Mo^{6+} (~232.7 eV/235.9 eV) [44]. After Zr doping, the average valence state of Mo in SFCMZ sample decreases from 5.35 to 5.28. The B-site cations of CoFe@SFCMZ change to lower valence states, leading to an increase in oxygen vacancy concentration according to the principle of electrical neutrality. Fig. S3d (Supporting information) shows the fitting spectra of Zr 3d orbitals, and the spin splitting peaks of Zr^{4+} $3d_{5/2}$ (180.6 eV) and Zr^{4+} $3d_{3/2}$ (182.9 eV) orbitals can be observed, further confirming that Zr is successfully doped into the SFCM lattice [45]. The distribution of various valence states of Fe, Co and Mo elements are shown in Tables S2~S4 (Supporting information).

From the thermogravimetric analysis (TGA) curves of CoFe@SFCMZ and CoFe@SFCM samples under Ar atmosphere shown in Fig. 3b, the weight loss of CoFe@SFCMZ is higher than that of CoFe@SFCM mainly due to the oxygen ions overflowing the lattice in the form of oxygen, and more weight loss means a higher oxygen vacancy concentration [46]. Besides, electron paramagnetic resonance (EPR) is used to further investigate the oxygen vacancies in both samples (Fig. 3c) [47]. CoFe@SFCMZ has a higher peak intensity, indicating a higher concentration of oxygen vacancies. In addition, the oxygen ion diffusion capabilities of two samples are studied by electrical conductivity relaxation (ECR). Fig. 3d shows the normalized conductivity versus time curves for two materials at 700 °C. Due to the increased concentration of oxygen vacancies, CoFe@SFCMZ exhibits an obviously shorter equilibrium time and a higher calculated oxygen ion diffusion coefficient ($D_{O,chem}$) of 3.97×10^{-5} cm^2/s, while the $D_{O,chem}$ of CoFe@SFCM is 1.74×10^{-5} cm^2/s. Furthermore, CoFe@SFCMZ also presents an increased proton diffusion coefficient ($D_{H,chem}$) of

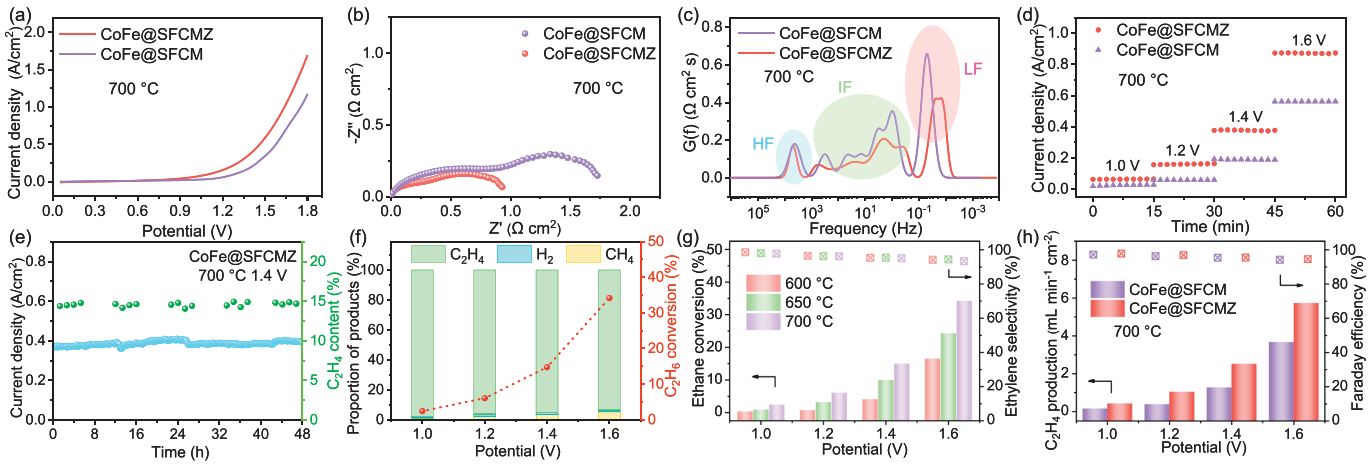

Fig. 4. (a) LSV curves of C_2H_6 electrolysis by CoFe@SFCMZ and CoFe@SFCM cells at 700 °C. (b) EIS and (c) DRT curves of both cells at 700 °C. (d) Short-term stability of both cells at different voltages at 700 °C. (e) Long-term stability of CoFe@SFCMZ cell. (f) Ethane conversion and proportion of products in the anode of CoFe@SFCMZ cell at 700 °C. (g) Ethane conversion and ethylene selectivity at 600, 650 and 700 °C and at different voltages for CoFe@SFCMZ cell. (h) C_2H_4 yield and Faraday efficiency of both cells at 700 °C.

9.76×10^{-7} cm^2/s at 700 °C, which is approximately three times than that of CoFe@SFCM (3.27×10^{-7} cm^2/s), as shown in Figs. 3e and f. The significant improvement suggests that Zr doping is an effective method to increase proton defects and promote fast proton diffusion [35]. The schematic diagram of the hydration reaction is shown in Fig. 3g. Because SFCMZ is a typical p-type semiconductor, its conductivity is primarily achieved through the movement of holes ($h^{\cdot}$) on B–O–B bonds [48]. During the hydration reaction ($H_2O + V_O^{\cdot\cdot} + O_O^{\times} \leftrightarrow 2OH_O^{\cdot}$), the O in water molecule combines with an oxygen vacancy on the surface of SFCMZ, forming lattice oxygen and holes ($O + V_O^{\cdot\cdot} \leftrightarrow O_O^{\times} + 2h^{\cdot}$). Meanwhile, the H in water molecule bind with $h^{\cdot}$ to form protons ($2H + 2h^{\cdot} \leftrightarrow 2H^{+}$), which are bound to the lattice oxygen to form $OH_O^{\cdot}$. However, oxygen ions in the lattice oxygen migrate faster than the protons, elucidating why conductivity initially rises followed by a decrease when water partial pressure increases. Until the concentrations of $h^{\cdot}$, $V_O^{\cdot\cdot}$ and $OH_O^{\cdot}$ are uniform throughout the sample, the hydration reaction reaches equilibrium [35].

The EENDH performance of CoFe@SFCMZ and CoFe@SFCM anodes are evaluated by analyzing the electrolytic curves. Fig. 4a shows the linear sweep voltammetry (LSV) curves of CoFe@SFCMZ and CoFe@SFCM cells at 700 °C. The current density of CoFe@SFCMZ cell reaches 0.87 A/cm^2 at 1.6 V, while the current density of CoFe@SFCM cell is only 0.56 A/cm^2 under the same condition. Meanwhile, to evaluate the effect of operation temperature, the electrolytic curves of CoFe@SFCMZ cells are also tested at different temperatures. As shown in Fig. S6 (Supporting information), the current densities of both cells increase with the rise of temperatures due to the enhanced reaction kinetics, and CoFe@SFCMZ cell exhibits higher current densities at each test temperature. In addition, the electrochemical performance of both anodes is extensively studied using electrochemical impedance spectroscopy (EIS). Fig. 4b shows the EIS spectra of CoFe@SFCMZ and CoFe@SFCM cells at 700 °C. The polarization impedance (R_p) value of CoFe@SFCMZ cell is only 0.98 Ω cm^2, while R_p value of CoFe@SFCM cell is 1.84 Ω cm^2, indicating that CoFe@SFCMZ anode has better electrocatalytic activity. The ohmic resistance is subtracted to show the change in polarization impedance more intuitively. Fig. 4c shows the relaxation time distribution (DRT) curves of CoFe@SFCMZ and CoFe@SFCM cells. The integrated peak areas of high-frequency (HF), intermediate frequency (IF) and low-frequency (LF) are related to the charge transfer process, the ion surface exchange process and the gas adsorption process, respectively [49]. The IF and LF peak areas of CoFe@SFCMZ cell are significantly smaller than those in CoFe@SFCM cell, indicating that Zr doping greatly promotes the surface ion exchange process and gas diffusion adsorption activation process.

Fig. 4d illustrates the short-term stability of the two cells under the electrolysis voltages of 1.0, 1.2, 1.4 and 1.6 V at 700 °C, indicating that both cells can stably work for 15 min at each voltage. And the current density of CoFe@SFCMZ cell at each voltage exceeds that of CoFe@SFCM cell, showing that CoFe@SFCMZ cell has a better ethane electrolysis performance. Moreover, long-term stability testing of CoFe@SFCMZ cell is also conducted at 700 °C, as shown in Fig. 4e. At a constant voltage of 1.4 V, the current density of CoFe@SFCMZ cell remains relatively stable at around 0.4 A/cm^2 over 48 h Additionally, the anode gas composition tested by gas chromatographic reveals no noticeable decline in the proportion of ethylene, proving that the electrocatalytic performance of the cell can also maintain stable over prolonged operation. In Fig. S8 (Supporting information), the cell structure is clear and the components are still well combined, which indicates that the electrodes and electrolyte have compatibility after stability test. CoFe@SFCMZ particles remain basically unchanged without significant carbon deposition. The *ex-situ* Raman measurement is also performed (Fig. S9 in Supporting information). There are no peaks at ~1330 cm^{-1} (D band) and ~1560 cm^{-1} (G band) assigned to carbon, indicating the resistance of heterogeneous structures to carbon deposition.

Furthermore, the ethane conversion and product composition in the anode of CoFe@SFCMZ and CoFe@SFCM cells at 700 °C are presented in Fig. 4f and Fig. S10 (Supporting information). For clarity, the proportion of components is the proportion other than the unreacted ethane. The ethane conversion rates of CoFe@SFCMZ cell at electrolysis voltages of 1.0, 1.2, 1.4 and 1.6 V are 2.46%, 6.07%, 14.98% and 34.22%, respectively, while for CoFe@SFCM cell at the same voltages, the conversion rates are only 0.93%, 2.30%, 7.52%, and 22.01%, respectively. The presence of H_2 proves that the thermal cracking of ethane occurs, but its content is very small, indicating that the electrochemical conversion of ethane is the main reason for the increase in the conversion rate. Additionally, the product contains a small amount of methane, which may originate from the C–C bond cleavage of ethane under high currents [20]. Zr doping increases the current density and proton migration rate of CoFe@SFCMZ cell, resulting in a significant increase in conversion rate. Fig. 4g shows the ethane conversion and ethylene selectivity of CoFe@SFCMZ cell under 600, 650 and 700 °C and at different voltages, with selectivity above 93% in all cases.

Fig. 4h shows the ethylene yield and Faraday efficiency of CoFe@SFCMZ and CoFe@SFCM cells at 700 °C. CoFe@SFCMZ cell achieves an ethylene yield of 5.74 mL min^{-1} cm^{-2} and a Faradaic efficiency of 94.6% at 1.6 V, significantly higher than that of the CoFe@SFCM cell (3.68 mL min^{-1} cm^{-2} and 94.2%). Fig. S11 (Supporting information) shows the CO yield and Faraday efficiency of both cells at 700 °C. It can be observed that with increasing voltage, C_2H_4 and CO yields show significant increases, indicating that the yield is mainly related to the electrolysis current magnitude. Meanwhile, the Faradaic efficiencies remain high values and relatively constant with voltage changes, suggesting that the energy conversion efficiencies of both cells are excellent.

In summary, CoFe@SFCMZ is successfully synthesized and applied as PCECs anode for EENDH. Zr doping increases the oxygen vacancy concentration of the material and enhances proton conductivity. The formation of a metal-oxide heterostructure significantly enhances the catalytic activity, ethylene selectivity, and long-term stability of EENDH. Electrochemical performance testing reveals that the CoFe@SFCMZ cell exhibits excellent electrocatalytic capability for ethane, achieving a high electrolysis current density of 0.87 A/cm^2 at 700 °C and 1.6 V. The ethane conversion rate reaches 34.22% with a corresponding ethylene selectivity of 93.4%, significantly higher than that of the CoFe@SFCM cell. Additionally, continuous operation for 48 h at a constant voltage of 1.4 V and 700 °C shows no significant performance degradation, demonstrating excellent long-term stability of the CoFe@SFCMZ cell. These findings highlight the outstanding electrocatalytic performance and stability of the CoFe@SFCMZ anode, suggesting promising prospects for its application in PCECs for EENDH.

Declaration of competing interest

The authors declare that they have no known competing financial interests or personal relationships that could have appeared to influence the work reported in this paper.

CRediT authorship contribution statement

Yixin Lu: Writing – review & editing, Writing – original draft, Visualization, Software, Resources, Project administration, Data curation. **Minghan Qin:** Visualization, Methodology, Data curation. **Shixian Zhang:** Writing – review & editing, Validation. **Zhen Liu:** Writing – review & editing, Data curation. **Wang Sun:** Writing – review & editing, Supervision, Funding acquisition. **Zhenhua Wang:** Supervision, Methodology. **Jinshuo Qiao:** Supervision, Methodology. **Kening Sun:** Supervision, Methodology.

Acknowledgments

This work was financially supported by the National Natural Science Foundation of China (Nos. 52272190 and 22178023) and the National Key R&D Program of China (No. 2021YFB4001401).

Supplementary materials

Supplementary material associated with this article can be found, in the online version, at doi:10.1016/j.cclet.2024.110567.

References

[1] Y. Gao, L. Neal, D. Ding, et al., ACS Catal. 9 (2019) 8592–8621.
[2] P. Wang, X. Zhang, R. Shi, et al., Nat. Commun. 15 (2024) 789.
[3] O. Mynko, I. Amghizar, D.J. Brown, et al., J. Clean Prod. 362 (2022) 132127.
[4] T. Ren, M. Patel, K. Blok, Energy 31 (2006) 425–451.
[5] S. De, S. Ould-Chikh, A. Aguilar, et al., ACS Catal. 11 (2021) 3988–3995.
[6] L. Ye, X. Duan, K. Xie, Angew. Chem. 133 (2021) 21914–21918.
[7] A. Al-Mamoori, S. Lawson, A.A. Rownaghi, et al., Appl. Catal. B: Environ. 278 (2020) 119329.
[8] X. Zhang, L. Ye, H. Li H, et al., ACS Catal. 10 (2020) 3505–3513.
[9] L. Wang, Y. Zhang, J. Xu, et al., Appl. Catal. B: Environ. 256 (2019) 117816.
[10] J.J. Sattler, J. Ruiz-Martinez, E. Santillan-Jimenez, et al., Chem. Rev. 114 (2014) 10613–10653.
[11] X. Zhang, B. Liu, Y. Yang Y, et al., Chin. Chem. Lett. 34 (2023) 108035.
[12] C. Fang, Y. Huang, K. Xu, et al., J. Power Sources 614 (2024) 234984.
[13] Y. Wang, Y. Ling, B. Wang, et al., Energy Environ. Sci. 16 (2023) 5721–5770.
[14] F. Liu, D. Ding, C. Duan, Adv. Sci. 10 (2023) 2206478.
[15] L. Ye, K. Xie, J. Energy Chem. 54 (2021) 736–745.
[16] L. Wang, Y. Fan Y, J. Li, et al., Ceram. Int. 47 (2021) 24106–24114.
[17] D. Ding, Y. Zhang, W. Wu, et al., Energy Environ. Sci. 11 (2018) 1710–1716.
[18] J. Luo, Y. Liu, J. Zhu J, et al., Chin. Chem. Lett. (2024), doi:10.1016/j.cclet.2024.110171.
[19] J. Sun, R. Ren, H. Yue, et al., Chin. Chem. Lett. 34 (2023) 107776.
[20] H. Sun, X. Xu, Y. Song, et al., Adv. Funct. Mater. 34 (2024) 2411622.
[21] P. Qiu, S. Sun, J. Li, et al., Sep. Purif. Technol. 298 (2022) 121581.
[22] Y. Fan, X. Xi, J. Li, et al., J. Am. Ceram. Soc. 105 (2022) 3613–3624.
[23] X. Gao, L. Ye, K. Xie, J. Power Sources 561 (2023) 232740.
[24] H. Lv, L. Lin, X. Zhang, et al., J. Mater. Chem. A 7 (2019) 11967–11975.
[25] T. Wei, P. Qiu, L. Jia L, et al., J. Mater. Chem. A 8 (2020) 9806–9812.
[26] M. Ma, X. Yang, C. Xu, et al., Sep. Purif. Technol. 296 (2022) 121411.
[27] J. Lv, W. Sun, C. Xu, et al., Sep. Purif. Technol. 294 (2022) 121127.
[28] M. Qin, S. Zhang, W. Sun, et al., Ceram. Int. 49 (2023) 30178–30186.
[29] L. Song, Y. Qiao, Y. Zhao, et al., Ceram. Int. 50 (2024) 24987–24994.
[30] C. Duan, J. Huang, N. Sullivan, et al., Appl. Phys. Rev. 7 (2020) 011314.
[31] X. Xu, Y. Xu, J. Ma, et al., J. Power Sources 489 (2021) 229486.
[32] R. Zohourian, R. Merkle, G. Raimondi, et al., Adv. Funct. Mater. 28 (2018) 1801241.
[33] Y. Gao, M. Zhang, M. Fu, et al., Energy Rev. 2 (2023) 100038.
[34] S. Zhang, W. Sun, C. Xu, et al., ACS Sustain. Chem. Eng. 12 (2024) 2289–2299.
[35] R. Ren, Z. Wang, X. Meng, et al., ACS Appl. Energ. Mater. 3 (2020) 4914–4922.
[36] C. Xu, W. Sun, R. Ren, et al., Appl. Catal. B: Environ. 282 (2021) 119553.
[37] H. Lv, Y. Zhou, X. Zhang, et al., J. Energy Chem. 35 (2019) 71–78.
[38] W. Fan, Z. Sun, Y. Bai, et al., ACS Appl. Mater. Interfaces 11 (2019) 23168–23179.
[39] K.D. Kreuer, Chem. Mat. 8 (1996) 610–641.
[40] Y. Li, Y. Li, Y. Wan Y, et al., Adv. Energy Mater. 9 (2019) 1803156.
[41] X. Xi, Z. Cao, X. Shen, et al., J. Power Sources 459 (2020) 228071.
[42] W. Zhang, H. Wang, K. Guan, et al., ACS Appl. Mater. Interfaces 11 (2019) 26830–26841.
[43] W. Zhang, H. Wang, K. Guan, et al., ACS Appl. Mater. Interfaces 12 (2019) 461–473.
[44] Z. Du, H. Zhao, S. Yi, et al., ACS Nano 10 (2016) 8660–8669.
[45] X. Ma, P. Lu, P. Wu, Ceram. Int. 44 (2018) 15989–15994.
[46] X. Kuai, G. Yang, Y. Chen, et al., Adv. Energy Mater. 9 (2019) 1902384.
[47] J. Yang, S. Hu, Y. Fang, et al., ACS Catal. 9 (2019) 9751–9763.
[48] Q. Liu, X. Dong, G. Xiao G, et al., Adv. Mater. 22 (2010) 5478–5482.
[49] B.A. Boukamp, A. Rolle, Solid State Ionics 314 (2018) 103–111.